

A likelihood method to cross-calibrate air-shower detectors

H.P. Dembinski,^{1,2} B. Kégl,³ I.C. Mariş,⁴ M. Roth,¹ and D. Veberič^{3,1}

¹Karlsruhe Institute of Technology

²University of Delaware

³Laboratoire de l'Accélérateur Linéaire

⁴Universidad de Granada

We present a detailed statistical treatment of the energy calibration of hybrid air-shower detectors, which combine a surface detector array and a fluorescence detector, to obtain an unbiased estimate of the calibration curve. The special features of calibration data from air showers prevent unbiased results, if a standard least-squares fit is applied to the problem. We develop a general maximum-likelihood approach, based on the detailed statistical model, to solve the problem. Our approach was developed for the Pierre Auger Observatory, but the applied principles are general and can be transferred to other air-shower experiments, even to the cross-calibration of other observables. Since our general likelihood function is expensive to compute, we derive two approximations with significantly smaller computational cost. In the recent years both have been used to calibrate data of the Pierre Auger Observatory. We demonstrate that these approximations introduce negligible bias when they are applied to simulated toy experiments, which mimic realistic experimental conditions.

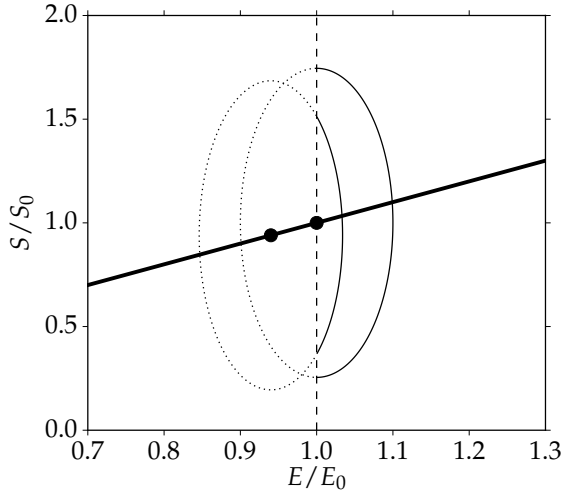


Figure 1. Sketch of the bias introduced by a simple energy cut. Shown is an ideal calibration curve $S \propto E$ of the size S of an air shower against its energy E (thick solid line), together with a low energy cut at E_0 . Measured estimates of E and S fluctuate around the true values and spread events from an ideal point on the calibration curve (black dots) outwards into an uncertainty ellipse. The line density of events on the ellipse is constant. Events that migrate below the cut are discarded (dotted arc). Surviving events (thin solid arc) spread more often below the ideal calibration curve since the arc is longer. A least-squares fit wrongly compensates this by placing the calibration curve below the true curve.

I. INTRODUCTION

The latest generation of air-shower detectors, the Pierre Auger Observatory [1, 2] and Telescope Array [3], are hybrid instruments. They combine a fluorescence detector which measures the calorimetric energy of an

air shower with a low duty cycle, and a surface detector array measuring its size at ground with a full duty cycle.

The size of an air shower measured at the same point in its longitudinal development is proportional to a power of its energy [4]. Therefore, a calibration function returning an energy estimate for a measured size can be found by analyzing a subset of coincident events recorded in both detectors.

Fitting the calibration function to pairs of energy and size estimates with a plain least-squares method yields biased results for several reasons. Firstly, the least-squares approach requires the true energy of the air shower to be known event-by-event, but the fluorescence detector only provides an energy estimate that fluctuates around the true energy. Secondly, the energy spectrum of cosmic rays is very steep so that most of the data is located near the lower energy threshold of the detector.

In the threshold region, the detector triggers are not fully efficient. Upward fluctuations have a higher chance of passing the trigger and entering the data set than downward fluctuations. This creates an acceptance bias, so that the mean size of the accepted events does not reflect the true mean size of the original sample.

Applying an energy cut with a minimum energy high enough to avoid the threshold region altogether solves this problem, but it creates a new bias, caused by event migration over the new threshold introduced by the cut. How the bias appears is illustrated in Fig. 1. A superficial solution is to use a slanted cut, but determining the angle under realistic conditions, where the resolutions vary with energy and size of the air shower, requires Monte-Carlo simulation of the data [5].

We will show that a probabilistic approach solves the problem in a consistent way. Based on the known properties of air-shower development and the detectors, we

construct a probability density model for the experimental data. Maximizing the likelihood of the data under this model then yields an asymptotically unbiased estimate of the calibration curve.

II. DEFINITION OF VARIABLES

We use the variable S for the size of the air shower at the ground, where it is observed by surface detector arrays. The size S depends on the energy E of the air shower, mass A , and geometry \mathbf{a} . We use air-shower geometry as a summary term for the orientation and impact point of the air-shower axis. The size S is often obtained by fitting an empirical lateral distribution function to the ground signals [6, 7], but other proxies work as well, such as the inferred total number of muons at ground in very inclined showers [8].

Air showers with the same geometry \mathbf{a} and energy E show a fluctuating size S at the ground. These fluctuations [9–11] are caused by random outcomes of the first few interactions of the air-shower development and possibly from sampling a random mass A from the mass-distribution of cosmic rays. The mass A is usually not exactly known event-by-event and therefore the dependency $\tilde{S}(A)$ adds to the observed fluctuations of S . We call these fluctuations combined *intrinsic fluctuations*.

Our aim is to find the function that yields the mean size \tilde{S} of the air shower, averaged over intrinsic fluctuations, as a function of its energy E and geometry \mathbf{a} . The energy dependence is usually modeled well by a power law $p_0 E^{p_1}$. Our approach does not depend on the exact relationship and therefore we will just refer to \mathbf{p} as the parameter vector of the function $\tilde{S}(E, \mathbf{a}, \mathbf{p})$.

We mention the dependence of \tilde{S} on the full air-shower geometry \mathbf{a} to treat the most general case. In practice, the dependency on \mathbf{a} is usually corrected before applying the energy calibration. The correction is either based on air-shower simulations [7, 8], or inferred from data, by demanding that the flux of cosmic rays looks isotropic in the corrected size [12].

The inverse of $\tilde{S}(E)$ serves as the energy calibration function, which provides an energy estimate E_S based on a size S of the air shower. Care must be taken, however, since the random fluctuations of the observed size propagate into the energy estimate. Analyses based on E_S need to take into account, that E_S randomly fluctuates around the true energy E event-by-event, combined with the fact that true energies follow a very steeply falling distribution. This makes it more likely that a particular observed value of E_S was generated by an upward fluctuation of an air-shower of lower energy, than by one with the same or higher energy. If the distribution of energies E is to be measured based on E_S [6], unfolding methods can be used [14, 15].

In addition to the effects discussed before, detectors do not measure the energy E , size S , and geometry \mathbf{a}

of the air shower directly. They provide estimates \hat{E} , \hat{S} , and $\hat{\mathbf{a}}$, that randomly fluctuate around the true values. These fluctuations are caused by statistical sampling of air-shower particles in the detector and by variations in the detector response. An experiment therefore provides a sample of tuples $(\hat{E}_i, \hat{S}_i, \hat{\mathbf{a}}_i)$ as input for the analysis. We assume that an energy cut $\hat{E} > E_{\text{cut}}$ is applied to this set which discards events with poor resolution in the threshold region of the detector.

To distinguish between functions and probability density functions (pdfs) in this article, we use the semi-colon in pdfs to separate the random variables from the dependent variables. For example, $f(x; p)$ is the probability density function f of the random variable x , whose location and shape depends on p . When integrals over random variables appear, we will not explicitly indicate the limits, except if the integral does *not* cover the physical domain of the variable, for example, $[0, \infty)$ for E and S .

We will refer to the normal distributions frequently, and therefore use the notation $\mathcal{N}(x; \mu, \sigma)$ to indicate the density

$$\mathcal{N}(x; \mu, \sigma) = \frac{1}{\sqrt{2\pi}\sigma} \exp\left(-\frac{1}{2}\left(\frac{x - \mu}{\sigma}\right)^2\right). \quad (1)$$

In a fully rigorous treatment, we would have to use the truncated normal distribution in most places, where the domain of the variable x is not the full real line. We generally assume that the experimental conditions are such that $\mu/\sigma \gg 0$, so that both distributions approach each other.

III. LIKELIHOOD ESTIMATION OF THE CALIBRATION FUNCTION

Our fitting method is based on the maximum-likelihood method [13]. For un-binned continuous data, it states that an estimate of the parameter vector \mathbf{p} can be found by maximizing the joint pdf \mathcal{L} of the data under the model considered. We make a usual substitution and maximize $\ln \mathcal{L}$ instead of \mathcal{L} ,

$$\ln \mathcal{L}(\mathbf{p}) = \sum_i \ln f(\hat{E}_i, \hat{S}_i, \hat{\mathbf{a}}_i; \mathbf{p}), \quad (2)$$

which is equivalent but easier to handle. The density $f(\hat{E}, \hat{S}, \hat{\mathbf{a}}; \mathbf{p})$ models the data distribution as a function of \mathbf{p} . We maximize this sum with standard numerical algorithms to get an estimate $\hat{\mathbf{p}}$ of \mathbf{p} .

If the data density was very high, working with a histogram of the data would be more effective and the log-likelihood would take a different form. Both approaches can also be combined, so that the former is used in high density regions to speed up the computation of the sum, an example of such a technique is given in Ref. [15].

The maximum-likelihood approach has a useful property that we will exploit repeatedly. Finding the maximum of $\ln \mathcal{L}$ to get the estimate $\hat{\mathbf{p}}$ only involves the first derivative $\nabla_{\mathbf{p}} \ln \mathcal{L}$. Similarly, computing the uncertainty estimate of $\hat{\mathbf{p}}$ only involves the second derivative. Therefore, any constant factors c_i with $\nabla_{\mathbf{p}} c_i = 0$, that appear in the evaluation of $f_i(\mathbf{p}) = f(\hat{E}_i, \hat{S}_i, \hat{\mathbf{a}}_i; \mathbf{p})$, can be dropped without changing these results,

$$\begin{aligned} \ln \mathcal{L}(\mathbf{p}) &= \sum_i \ln f_i(\mathbf{p}) = \sum_i \ln c_i f'_i(\mathbf{p}) \\ &= \sum_i \ln c_i + \sum_i \ln f'_i(\mathbf{p}) \equiv \sum_i \ln f'_i(\mathbf{p}). \end{aligned} \quad (3)$$

We will use this to avoid the explicit computation of such factors wherever possible.

We now focus on the construction of $f(\hat{E}, \hat{S}, \hat{\mathbf{a}}; \mathbf{p})$. The size function $\bar{S}(E, \mathbf{a}, \mathbf{p})$ of the air-shower is at the heart of this pdf, the crucial point is to model the random fluctuations of events around this mean.

A. Statistical model of the detection process

The pdf $f(\hat{E}, \hat{S}, \hat{\mathbf{a}}; \mathbf{p})$ of the observed ensemble is constructed by folding several conditional pdfs that model the individual sources of fluctuations with the pdf $h(E, \mathbf{a})$ of the arrival frequencies of air showers at the combined aperture of the detectors. The pdf $h(E, \mathbf{a})$ itself is obtained by normalizing the product of the cosmic-ray flux $J(E) = dN/(dE dA dt d\Omega)$ with the effective aperture $A_{\text{eff}}(E, A, \mathbf{a})$ of the combined detectors. The effective aperture can depend on energy and mass of the cosmic ray. For example, a fluorescence telescope can see high-energy air showers from a greater distance, since they are brighter. We emphasize that for the energy calibration to work, any mass dependency in the effective aperture of the calibration data needs to be the same as in the final data set to be calibrated.

We now introduce the fluctuations step-by-step. If the detectors were perfect and there were no intrinsic fluctuations, we would describe the data with distribution

$$f_1(E, S, \mathbf{a}; \mathbf{p}) = \delta(S - \bar{S}(E, \mathbf{a}, \mathbf{p})) h(E, \mathbf{a}), \quad (4)$$

where the Dirac δ -distribution states that the observed values follow the function $\bar{S}(E, \mathbf{a}, \mathbf{p})$ exactly. Yet, certain pairs of \bar{S} and E occur more frequently than others, due to the different arrival frequencies of air showers, quantified by $h(E, \mathbf{a})$. For a fixed geometry \mathbf{a} , Eq. (4) represents a line density embedded into the (E, S) plane. It traces the function $\bar{S}(E, \mathbf{a}, \mathbf{p})$ that we want to extract.

By modeling how events are randomly scattered away from the line density, we develop the connection between the function $\bar{S}(E, \mathbf{a}, \mathbf{p})$ and the observed ensemble. Intrinsic fluctuations are incorporated by re-

placing the δ -distribution with a conditional pdf s , obtaining

$$f_2(E, S, \mathbf{a}; \mathbf{p}) = s(S; \bar{S}(E, \mathbf{a}, \mathbf{p}), E, \mathbf{a}) h(E, \mathbf{a}). \quad (5)$$

The shape of the pdf s itself can depend on the air-shower energy E and the geometry \mathbf{a} .

Now we add fluctuations caused by the detectors, and regard event loss from online triggers and a minimum energy cut. These effects are modeled by another conditional probability density function, the detector kernel $g(\hat{E}, \hat{S}, \hat{\mathbf{a}}; E, S, \mathbf{a})$. We fold f_2 with the kernel and multiply the result with a Heaviside function $\Theta(\hat{E} - E_{\text{cut}})$ to model the effect of the applied energy cut. This yields our first main result

$$\begin{aligned} f_3(\hat{E}, \hat{S}, \hat{\mathbf{a}}; \mathbf{p}) &= \Theta(\hat{E} - E_{\text{cut}}) \int dE \int dS \int d\mathbf{a} \\ &g(\hat{E}, \hat{S}, \hat{\mathbf{a}}; E, S, \mathbf{a}) f_2(E, S, \mathbf{a}; \mathbf{p}). \end{aligned} \quad (6)$$

We neglect here, that shower-to-shower fluctuations in the size S may be accompanied by anti-correlated fluctuations in the energy estimate \hat{E} . The energy estimate \hat{E} is typically based on light generated primarily by the electromagnetic cascade. A fraction of the shower-to-shower fluctuations is caused by variations in the flow of cosmic-ray energy into the hadronic and electromagnetic cascade. The anti-correlations reflect the conservation of energy. Anti-correlated fluctuations in the energy estimate are expected to be smaller than 4% above 10^{18} eV, and decreasing at higher energies [16]. This is typically small compared to the energy resolution, and therefore not included in the model.

Apart from this simplification, Eq. (6) is a general statistical model of the calibration data. The detector kernel $g(\hat{E}, \hat{S}, \hat{\mathbf{a}}; E, S, \mathbf{a})$ can be obtained from Monte-Carlo simulation or derived from an empirical model. The pdf s needs to be estimated from air-shower simulations or fitted to the calibration data together with the function $\bar{S}(E, \mathbf{a}, \mathbf{p})$.

Due to losses modeled by the Heaviside function and the detector kernel, f_3 is not normalized to unity. The maximum-likelihood method does not require f_3 to be normalized, if the normalization does not depend on the parameters \mathbf{p} that are optimized. Otherwise, f_3 needs to be replaced by

$$f(\hat{E}, \hat{S}, \hat{\mathbf{a}}; \mathbf{p}) = \frac{f_3(\hat{E}, \hat{S}, \hat{\mathbf{a}}; \mathbf{p})}{\int d\hat{E} \int d\hat{S} \int d\hat{\mathbf{a}} f_3(\hat{E}, \hat{S}, \hat{\mathbf{a}}; \mathbf{p})}. \quad (7)$$

A numerical computation of the normalization is expensive and should be avoided. We will show how the computation can be neglected in good approximation if a sufficiently large value of E_{cut} is chosen in the next section.

Our approach in its general form is more complex than a plain least-squares fit of the data, but if it is a complete probabilistic model of the data, maximizing

the likelihood of the data under the model is guaranteed to yield an asymptotically unbiased estimate of the calibration curve. In particular, the probabilistic model handles inefficiencies and event migration above the threshold defined by the energy cut E_{cut} , which cannot be dealt with in the framework of least-squares fitting.

The general form of Eq. (6) is expensive to compute due to the many integrals. We will proceed to discuss valid approximations which greatly reduce the computational cost, up to a point of removing all integrals. We will illustrate these approximations along an fully fledged example: the application of the likelihood approach to the energy calibration in the Pierre Auger Observatory.

IV. APPLICATION TO THE PIERRE AUGER OBSERVATORY

Two variants of our approach have been used in recent analyses from the Pierre Auger Observatory. The variants are obtained by approximating Eq. (7) in a controlled manner, which reduces it into a practical form.

Both variants have a few aspects in common. The Auger surface detector array is sufficiently flat and regular, so that the dependence on the air-shower geometry \mathbf{a} reduces only to a dependence on the zenith angle θ . The remaining atmospheric attenuation is corrected either empirically by demanding flux isotropy [12, 19] or based on air-shower simulations [18]. Thus, in this case the refined size parameter S depends only on the energy E of the air-shower, and we have

$$\bar{S}(E) = p_0 E^{p_1}. \quad (8)$$

A. Detector kernel

The detector kernel is factorized into two independent normal distributions for \hat{E} and \hat{S} , and a δ -distribution for $\hat{\theta}$,

$$g(\hat{E}, \hat{S}, \hat{\theta}; E, S, \theta) \approx g_{\hat{E}}(\hat{E}; E) g_{\hat{S}}(\hat{S}; S, \theta) \delta(\hat{\theta} - \theta), \quad (9)$$

with

$$g_{\hat{E}}(\hat{E}; E) = \mathcal{N}(\hat{E}; E, \sigma_{\hat{E}}(E)) \quad (10)$$

$$g_{\hat{S}}(\hat{S}; S, \theta) = \mathcal{N}(\hat{S}; S, \sigma_{\hat{S}}(S, \theta)). \quad (11)$$

Using independent normal distributions for \hat{E} and \hat{S} is well motivated, since the measurements are practically independent. The measurements implicitly sum up many individual signals with near-normal distributions. Due to the central-limit theorem, the resolutions turn Gaussian.

Using the δ -distribution for $\hat{\theta}$ is an approximation that saves a numerical integration. The δ -distribution is the limit of a normal distribution with vanishing width,

so effectively this ansatz treats the measurement of θ as exact. For the Pierre Auger Observatory this approximation is very good, since the angular resolution is high and the detector kernel is only a slowly varying function of θ .

Event losses in the detector are neglected. This can be made into a good approximation by choosing a sufficiently high value of the energy cut E_{cut} . The value of E_{cut} needs to be high enough so that all accepted events have 100 % detection efficiency, and rejected events with a reasonable chance to migrate over the threshold still have efficiencies near 100 %.

Under these conditions, the normalization of Eq. (6) becomes independent of the choice of \mathbf{p} . Therefore, Eq. (6) can be used directly in the likelihood instead of Eq. (7). We will drop the Heaviside function $\Theta(\hat{E} - E_{\text{cut}})$ from now on, since it is always one for the selected data and was only needed to compute the normalization in the general case.

B. Intrinsic fluctuations

The pdf $s(S; \bar{S}, E)$ of the intrinsic fluctuations is modeled by a normal distribution

$$s(S; \bar{S}(E, \mathbf{p}), E, \mathbf{p}) = \mathcal{N}(S; \bar{S}(E, \mathbf{p}), \sigma_S(E)). \quad (12)$$

In case of the Pierre Auger Observatory, there is no indication that the shower-to-shower fluctuations depend on the air-shower geometry \mathbf{a} , so the dependency is dropped.

The choice of a normal distribution is only empirically motivated, since the pdf is theoretically unknown. Its shape depends on the unknown distribution of cosmic-ray masses. However, pure samples of simulated proton and iron air-showers show distributions close to normal [10], and the model fits data from the Pierre Auger Observatory well [17, 19].

C. Combined fluctuation model

Since both the detector-generated fluctuations ($\hat{S} - S$) and the intrinsic fluctuations ($S - \bar{S}$) are modeled by normal distributions, it is tempting to carry out the folding

$$g_s(\hat{S}) = \int dS g_{\hat{S}}(\hat{S}; S, \theta) s(S; \bar{S}(E, \mathbf{p}), E, \theta) \quad (13)$$

analytically, to save another numerical integration. Unfortunately, the trivial solution that holds for two independent normal distributions

$$g_s^N(\hat{S}) = \mathcal{N}(\hat{S}; \bar{S}(E, \mathbf{p}), (\sigma_{\hat{S}}^2 + \sigma_S^2)^{1/2}) \quad (14)$$

does not work here, since the resolution $\sigma_{\hat{S}}$ of the detector depends on the random outcome S from shower-to-shower fluctuations. The fluctuations are coupled.

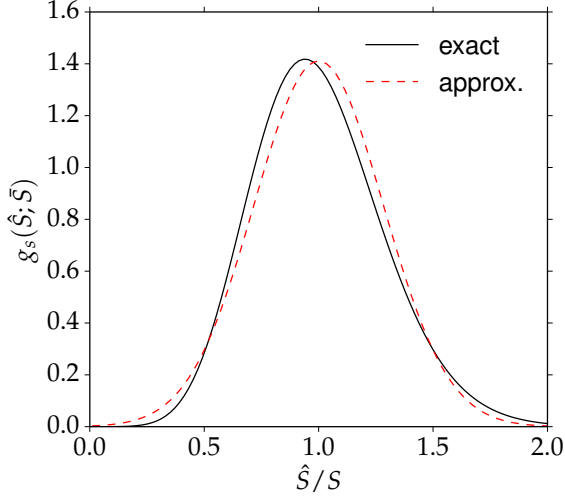


Figure 2. Exact solution $g_s(\hat{S}; \bar{S})$ and normal approximation $g_s^N(\hat{S}; \bar{S})$ to the folding of two normal distributions $g_{\hat{S}}(\hat{S} - S)$ and $s(S - \bar{S})$ with $\sigma_{\hat{S}}/S = \sigma_S/\bar{S} = 0.2$.

The difference between the normal approximation g_s^N , obtained by replacing S with \bar{S} in the computation of $\sigma_{\hat{S}}$, and the exact solution g_s is illustrated in Fig. 2 for realistic values of $\sigma_{\hat{S}}/S = \sigma_S/\bar{S} = 0.2$. The exact solution has a shape that resembles something between a normal and log-normal distribution, in agreement with early studies based on Monte-Carlo simulations of air showers [5].

The normal approximation g_s^N is nevertheless acceptable for the estimation of $\bar{S}(E, \mathbf{p})$, since g_s^N and g_s have the same expectation value, as pointed out in Appendix A. The maximum-likelihood estimator of the central value of g_s^N is unbiased with respect to the expectation value, and therefore this approximation does not bias the fit of the size function $\bar{S}(E, \mathbf{p})$.

However, the approximation biases the estimate of the width $\hat{\sigma}_S$ of the intrinsic fluctuations. While this parameter is irrelevant for the energy calibration itself, it has to be fitted to data since its true value is unknown. The width is also of physical interest in its own, since it is sensitive to the cosmic-ray mass composition. The impact on $\hat{\sigma}_S$ is shown in Section V.

By assembling all pieces together and carrying out the integration over θ , we arrive at the following form

$$f(\hat{E}, \hat{S}, \hat{\theta}; \mathbf{p}) = \int dE g_{\hat{E}}(\hat{E}; E) g_s^N(\hat{S}; E, \hat{\theta}, \mathbf{p}) h(E, \hat{\theta}). \quad (15)$$

This form is the common root of two variants which have been independently derived and used for different zenith angle ranges at the Pierre Auger Observatory. Both variants assume that the distribution of hybrid events $h(E, \theta)$ factorizes,

$$h(E, \theta) = h_E(E) h_{\theta}(\theta), \quad (16)$$

which follows if the effective aperture A_{eff} for hybrid events factorizes in these variables. This was found to hold in good approximation [10].

D. Variant A

In variant A, Eq. (15) is integrated over the estimated zenith angle $\hat{\theta}$, which effectively removes one dimension of the data from the likelihood and the inference. This variant has been used at the Pierre Auger Observatory to calibrate air showers with zenith angles up to 60° [19].

The integration leads to an effective kernel on the right hand side of Eq. (15)

$$\bar{g}_s^N(\hat{S}; E, \mathbf{p}) = \int d\hat{\theta} g_s^N(\hat{S}; E, \hat{\theta}, \mathbf{p}) h_{\theta}(\hat{\theta}), \quad (17)$$

which is again approximated by a normal distribution. This approximation is good where the zenith angle dependency of the detector kernel is weak.

The remaining partial distribution $h_E(E)$ is approximated by a power law $E^{-\gamma}$ with an appropriate spectral index. We arrive at variant A,

$$f_A(\hat{E}, \hat{S}; \mathbf{p}) = C \int dE \frac{1}{\sigma_E \tilde{\sigma}_{\hat{S}}} \times \exp \left(-\frac{1}{2} \left(\frac{\hat{E} - E}{\sigma_E} \right)^2 - \frac{1}{2} \left(\frac{\hat{S} - p_0 E^{p_1}}{\tilde{\sigma}_{\hat{S}}} \right)^2 \right) E^{-\gamma}, \quad (18)$$

where $\tilde{\sigma}_{\hat{S}}(E) = (\sigma_{\hat{S}}(p_0 E^{p_1})^2 + \sigma_S(E)^2)^{1/2}$ is an effective resolution that includes shower-to-shower fluctuations, and C is an unspecified normalization constant that does not depend on \mathbf{p} and is therefore irrelevant for the likelihood estimation.

The log-likelihood function then is (up to constants)

$$\ln \mathcal{L}_A(\mathbf{p}) = \sum_i \ln \int dE \frac{1}{\sigma_E \tilde{\sigma}_{\hat{S}}} \times \exp \left(-\frac{1}{2} \left(\frac{\hat{E}_i - E}{\sigma_E} \right)^2 - \frac{1}{2} \left(\frac{\hat{S}_i - p_0 E^{p_1}}{\tilde{\sigma}_{\hat{S}}} \right)^2 \right) E^{-\gamma}. \quad (19)$$

The integration over the true energy E is carried out numerically for each observed tuple (\hat{E}_i, \hat{S}_i) .

E. Variant B

In variant B, the approximations after Eq. (15) take a different path. The zenith angle dependency is kept, and a bootstrap estimate is used to remove the last remaining integral. The result is a double sum, which is fast to compute for small to moderate data sets. Variant B has been used to calibrate very inclined events with zenith angles beyond 65° [20].

We start by observing that the pdf $h_E(E)$ of hybrid events is well approximated by the pdf $h_{\hat{E}}(\hat{E})$ in the range of interest, which describes the distribution of the observed energy estimates \hat{E} . Both pdfs differ by an integration over the detector kernel $g_{\hat{E}}$ of the energy measurement,

$$h_{\hat{E}}(\hat{E}) = \int dE g_{\hat{E}}(\hat{E}; E) h_E(E). \quad (20)$$

The effect of the folding is small since the resolution of the energy measurement is about 10 % [2]. In particular, in the region near E_{cut} and above, the pdfs differ mainly by a shift that can be absorbed into the normalization.

After establishing this, we can now estimate the pdf $h_{\hat{E}}$ from the calibration data itself. This could be done with a kernel density estimate or another non-parametric density estimation method. Since $h_{\hat{E}}$ appears only inside an integral, we chose the even simpler bootstrap estimate [21]. The bootstrap estimate can be regarded as a kernel density estimate with a kernel of vanishing width. It is constructed as a sum of δ -distributions positioned at the observed values \hat{E}_k , weighted by the inverse of the overall detection efficiency $\epsilon_k = \epsilon(\hat{E}_k)$ at this value,

$$h_{\hat{E}}^B(\hat{E}) = \frac{1}{K} \sum_k \frac{\delta(\hat{E} - \hat{E}_k)}{\epsilon_k}. \quad (21)$$

The sum over k is independent of the sum in Eq. (2) and runs over all K hybrid events, not only those above the cut value E_{cut} .

Bootstrap theory is not well known in physics, but it is an established branch of statistics. For example, the sample mean can be derived as the bootstrap estimate of the expectation value for an arbitrary pdf $f(x)$

$$\begin{aligned} E[x] &= \int dx x f(x) \rightarrow E^B[x] = \int dx x f^B(x) \\ &= \int dx x \frac{1}{K} \sum_k \delta(x - x_k) = \frac{1}{K} \sum_k x_k. \end{aligned} \quad (22)$$

By inserting Eq. (21) into Eq. (15) and integrating over E , we obtain

$$\begin{aligned} f_B(\hat{E}, \hat{S}, \hat{\theta}; \mathbf{p}) &= \frac{h_{\theta}(\hat{\theta})}{2\pi K} \times \\ &\sum_k \frac{1}{\epsilon_k} \mathcal{N}(\hat{E}; \hat{E}_k, \sigma_{\hat{E},k}) \mathcal{N}(\hat{S}; p_0 \hat{E}_k^{p_1}, \tilde{\sigma}_{\hat{S},k}), \end{aligned} \quad (23)$$

with kernel width functions evaluated at the bootstrap values \hat{E}_k ,

$$\sigma_{\hat{E},k} = \sigma_{\hat{E}}(\hat{E}_k) \quad (24)$$

$$\tilde{\sigma}_{\hat{S},k} = \left(\sigma_{\hat{S}}(p_0 \hat{E}_k^{p_1}, \hat{\theta})^2 + \sigma_S(\hat{E}_k)^2 \right)^{1/2}. \quad (25)$$

A final approximation replaces the output of the kernel width functions $\sigma_{\hat{E}}$ and $\sigma_{\hat{S}}$ with their event-wise estimates $\hat{\sigma}_{\hat{E},k}$ and $\hat{\sigma}_{\hat{S},k}$ from the reconstruction algorithms.

This change is not strictly necessary, but it avoids the need to parametrize and fit the kernel width functions to data in advance. This leaves the efficiency function $\epsilon(\hat{E})$ as the only external input.

Inserting Eq. (23) into Eq. (2) yields a curious double sum over the energy estimates, caused by the bootstrap approximation. After dropping all constant factors that do not depend on \mathbf{p} , which includes $h_{\theta}(\hat{\theta})$, we obtain

$$\begin{aligned} \ln \mathcal{L}_B(\mathbf{p}) &= \sum_i \ln \left[\sum_k \frac{1}{\hat{\sigma}_{\hat{E},k} \hat{\sigma}_{\hat{S},k} \epsilon_k} \times \right. \\ &\left. \exp \left(-\frac{1}{2} \left(\frac{\hat{E}_i - \hat{E}_k}{\hat{\sigma}_{\hat{E},k}} \right)^2 - \frac{1}{2} \left(\frac{\hat{S}_i - p_0 \hat{E}_k^{p_1}}{\hat{\sigma}_{\hat{S},k}} \right)^2 \right) \right], \end{aligned} \quad (26)$$

where the sum over i only includes events with $\hat{E}_i > E_{\text{cut}}$. This is the final result of approximation B.

The structure of Eq. (26) allows for some optimization, which may make the numerical maximization of the log-likelihood faster. The matrix $z_{ik} = (\hat{E}_i - \hat{E}_k)/\sigma_{\hat{E},k}$ is constant with respect to changes in \mathbf{p} , and can be precomputed. Terms with $|z_{ik}| > 8$ can be discarded altogether, as their contributions to the second sum are negligible.

We note that Eq. (26) cannot be further reduced into an equivalent least-squares method due to the sum inside the logarithmic terms.

V. PERFORMANCE IN TOY SIMULATIONS

We test the frequentistic properties of our fits on a set of simulated experiments. We are particularly interested in the bias $E[\hat{\mathbf{p}} - \mathbf{p}]$ of the maximum-likelihood estimate $\hat{\mathbf{p}}$ and the true coverage of the estimated confidence region. We approximate the confidence region with an ellipsoid in the usual fashion, represented by the covariance matrix obtained after inverting the Hesse matrix of $-\ln \mathcal{L}(\mathbf{p})$.

In order to study these statistical properties, we simulate data sets of toy experiments. In these simple simulations data points are drawn from parametrized distributions, which mimic the experimental conditions for the detection of very inclined air showers at the Pierre Auger Observatory. The results obtained here hold equally well for a simulation of less inclined events. The parametrization were taken from a previous study [10] and are summarized in Appendix B. The distribution of hybrid events and the average event loss due to the simulated trigger is shown in Fig. 3.

We generate 1000 toy experiments. In each toy experiment, we generate events until 200 pass the energy cut $E_{\text{cut}} = 10^{18.6}$ eV. The true size function is taken to be

$$\bar{S}(E) = p_0 (E/10^{19} \text{ eV})^{p_1} \quad (27)$$

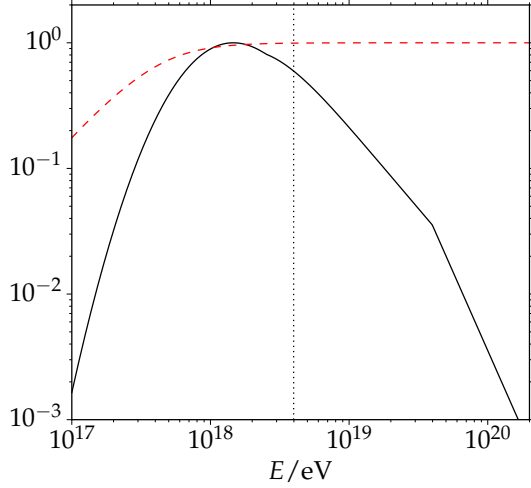


Figure 3. Energy distribution $dN/d\ln E$ of hybrid events (solid line) in arbitrary units and effective trigger efficiency (dashed line) used in the toy simulation. The minimum energy cut used in the fits is also indicated (dotted line).

with input values $\mathbf{p} = (2.0, 0.9)$.

We fit the toy data with both variant A and B, using Eq. (19) and Eq. (26), respectively. For each simulated experiment and variant, we obtain a parameter vector $\hat{\mathbf{p}}$. After fitting many independent experiments, the average $\langle \hat{\mathbf{p}} - \mathbf{p} \rangle$ will approach the bias.

In case of variant A, we insert the true resolution functions used in the toy simulation in the integrand of Eq. (19). The spectral index is set to $\gamma = -2.4$, based on a power law fit to the simulated hybrid distribution between $10^{18.5}$ eV and $10^{19.5}$ eV.

In case of variant B, we set the efficiencies $\epsilon_k = 1$ in Eq. (26) for simplicity, since the effective trigger efficiency does not depart significantly from one above 10^{18} eV. Only this region is potentially relevant for event migration above the energy cut.

Intrinsic fluctuations in the toy simulation have a constant relative resolution, $\sigma_S/\bar{S} = 0.15$. To obtain results that generalize well, we do not assume the same in the likelihood fits. In principle, the relative resolution could vary smoothly with energy, for example, if the mass composition changes with energy. Therefore, we model the intrinsic fluctuations with a second-order Bernstein polynomial,

$$\sigma_S/\bar{S} = q_0(1-z)^2 + q_1(1-z)z + q_2z^2 \quad (28)$$

$$z = \begin{cases} 0 & ; \text{if } E < 10^{18} \text{ eV} \\ \frac{\lg(E/10^{18} \text{ eV})}{\lg(10^{20} \text{ eV}/10^{18} \text{ eV})} & ; \text{if } 10^{18} \text{ eV} < E \leq 10^{20} \text{ eV} , \\ 1 & ; \text{if } E > 10^{20} \text{ eV} \end{cases}$$

and fit the three parameters \mathbf{q} along with the parameters \mathbf{p} to each data set. The parametrization with a

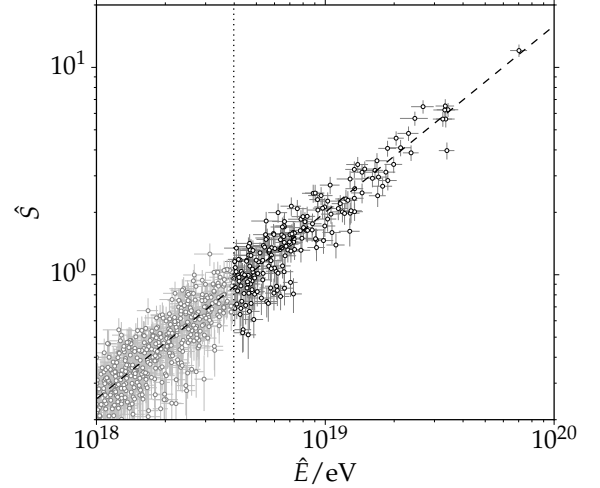


Figure 4. Simulated data (circles with error bars) from one toy experiment. Also shown are the true mean size \bar{S} (dashed line) of the air showers and the energy cut at $10^{18.6}$ eV (dotted line).

Bernstein polynomial allows us to implement the physical constraint $\sigma_S > 0$ with a simple lower limit $q_\ell > 0$ on the parameters, supported by most numerical optimization algorithms.

While the intrinsic fluctuations are not of primary interest for the calibration curve, they need to be fitted in order to complete the probabilistic model. Assuming that they are zero leads to a significant bias in the fitted parameters \mathbf{p} of the toy experiments. In addition, fitting the intrinsic fluctuations provides valuable physical information, since they are sensitive to the cosmic-ray mass composition [10, 11].

To put our likelihood methods in perspective, we also apply a naive least-squares fit, where $\hat{\mathbf{p}}$ is obtained by minimizing

$$\chi^2(\mathbf{p}) = \sum_i \left(\frac{\hat{S}_i - p_0 \hat{E}_i^{p_1}}{\hat{\sigma}_{\hat{S},i}} \right)^2, \quad (29)$$

where $\hat{\sigma}_{\hat{S},i}$ is the event-wise uncertainty estimate provided by the simulation.

One of the toy experiments is shown in Fig. 4. Only data points above the energy cut value E_{cut} enter the fits directly. In case of variant B, the data to the left is still used indirectly to construct the bootstrap estimate of $h_E(E)$, as described in the previous section.

A detailed comparison of the fit results for this data set is shown in Fig. 5, which in addition illustrates the dependence on the energy cut. The naive least-squares fit shows a large bias for any cut value in p_0 , while the likelihood variants appear unbiased for energy cuts higher than the nominal value and give very similar results. A consistent bias for energy cuts below 10^{18} eV

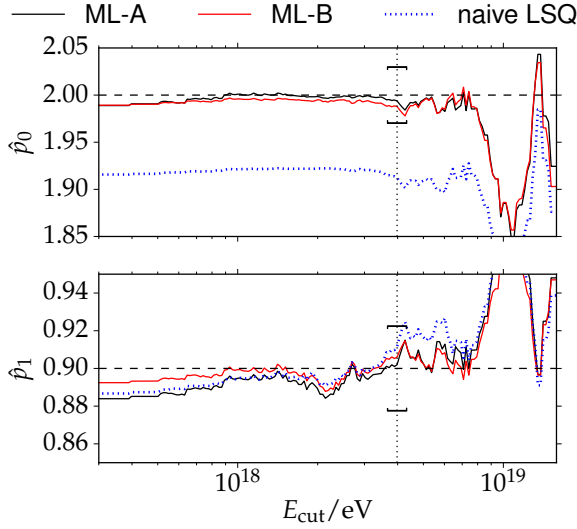


Figure 5. Fitted parameters for the data shown in Fig. 4 as a function of the energy cut value, from the likelihood fits (solid lines) and the naive least-squares fit (dotted line). The true parameter values from the simulation (dashed lines) and the nominal cut value are indicated (dotted vertical line). Brackets indicate the statistical uncertainty of the fit at the nominal cut value. The jitter is caused by the discreteness of the data set. It increases with the energy cut, since the number of accepted events decreases and the lever arm for the fit becomes shorter.

| | $\langle \hat{p}_0 \rangle, (\langle \hat{p}_0 - p_0 \rangle)$ | $\langle \hat{p}_1 \rangle, (\langle \hat{p}_1 - p_1 \rangle)$ |
|-----------|--|--|
| ML-A | $2.003 \pm 0.001 (+0.003)$ | $0.898 \pm 0.001 (-0.002)$ |
| ML-B | $1.998 \pm 0.001 (-0.002)$ | $0.898 \pm 0.001 (-0.002)$ |
| Naive LSQ | $1.910 \pm 0.001 (-0.090)$ | $0.892 \pm 0.001 (-0.008)$ |

Table I. Averages of the fitted parameters from 1000 toy experiments for the two likelihood fits and the naive least-squares fit. The estimated bias is shown in parentheses.

is also found for the likelihood fits. The jitter in the scans varies from experiment to experiment, but these biases appear consistently.

The bias in case of low energy cuts is expected, since the trigger efficiency begins to deviates significantly from one below 10^{18} eV, as shown in Fig. 3, and the selection bias due to the trigger becomes important. Since efficiency terms were taken out of the statistical model to obtain the approximations, the fits are not applicable at such low energy cuts.

The biases are further explored in Fig. 6 and Table I. The naive least-squares fit is strongly biased, while the observed bias in the two likelihood fits is negligible. The statistical uncertainties in a single toy experiment are an order of magnitude larger. The estimated confidence regions constructed from log-likelihood cover the true values in 66 % of the toy experiments for variant A and B, very close to the expected 68 %.

The fitted intrinsic fluctuations $\hat{\sigma}_S$ are shown in Fig. 7.

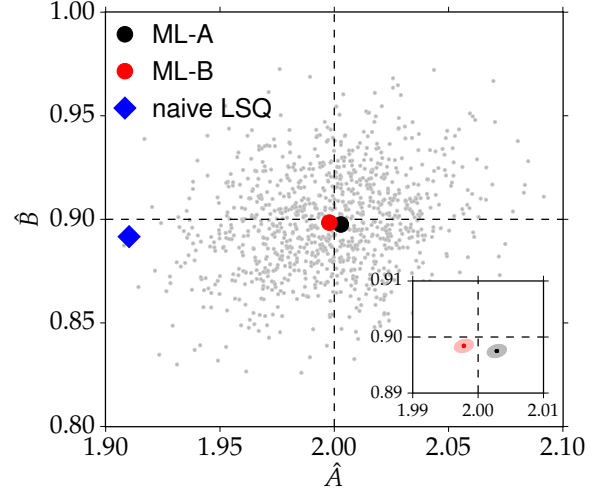


Figure 6. Averaged parameter estimates from 1000 toy experiments for the two likelihood fits (circles) and the naive least-squares fit (diamond), compared to the true values (dotted lines). Shown in the background are the individual outcomes obtained from variant B (small dots), those of variant A are very similar. The inset zooms closer to the true values. Ellipses around the average fitted values represent the statistical uncertainty of the average.

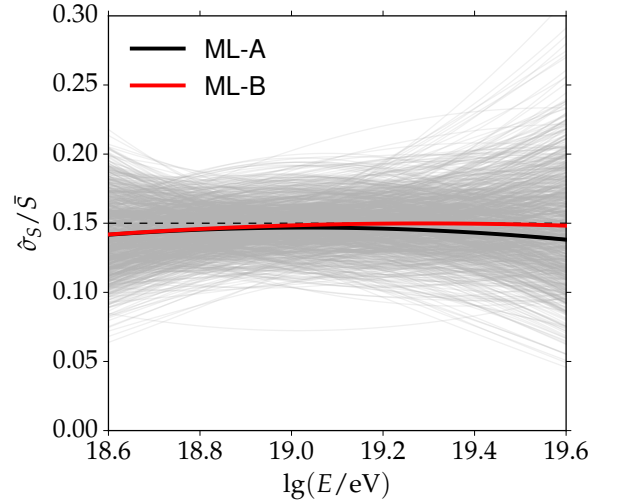


Figure 7. Averaged estimate of the intrinsic fluctuations $\hat{\sigma}_S/\bar{S}$ from 1000 toy experiments for the two likelihood fits (thick lines with error bands), compared to the true constant value (horizontal dots). Shown in the background are the individual outcomes obtained with variant B (thin lines), those of variant A are very similar.

Both likelihood fits show a small bias $\langle \hat{\sigma}_S / \bar{S} - \sigma_S / \bar{S} \rangle$ of about 10% below 10^{19} eV. At higher energies, variant B performs slightly better than variant A. The variation in the fit from experiment to experiment is large, however, especially at the high end of the energy range. The scatter at the high end reflects that the fit is less constrained where the data density is low. The interpretation of trends in the fitted fluctuations therefore has to be done carefully.

Further exploration showed that the bias vanishes, if the toy simulation is done with the normal approximation g_S^N to the combined fluctuation model instead of the correct computation. The bias is therefore a consequence of the normal approximation described in Section IV C.

In a final test, we push the bootstrap estimate of $h_{\hat{E}}(\hat{E})$ in variant B to the extreme by generating another set of 1000 toy experiments with only 10 events above E_{cut} . Again, we find only negligible bias in the parameters of the calibration curve.

VI. CONCLUSION

We presented a statistical model that describes data taken by a hybrid air-shower detector, consisting of a surface detector array, which measures a size of an air shower, and a fluorescence detector, which measures an energy estimator. We developed a maximum-likelihood approach based on the statistical model, which allows us to infer an asymptotically unbiased energy calibra-

tion curve for the size from coincident events observed in both detector parts.

Since the general model is somewhat cumbersome to use, we derived two approximations. The approximations lead to handy formulas, without sacrificing accuracy or introducing significant bias. Both approximations are used by the Pierre Auger Observatory in different zenith angle ranges.

We applied the more aggressive approximation to simulated toy experiments, to investigate the statistical performance. The results showed that the estimated calibration curves are not biased with respect to the true curve used in the generation of the toy data.

ACKNOWLEDGMENTS

We gratefully acknowledge the very fruitful exchanges we had with all of our colleagues in the Auger collaboration. The valuable discussions with Michael Unger need to be highlighted especially. This work was supported in part by the Helmholtz Alliance for Astroparticle Physics HAP, funded by the Initiative and Networking Fund of the Helmholtz Association, by the German Federal Ministry for Education and Research (BMBF), Grant 05A11VK1, and by the ANR-2010-COSI-002 grant of the French National Research Agency. I.C. Mariş acknowledges the financial support by the European Community 7th Framework Program, through the Marie Curie Grant FP7-PEOPLE-2012-IEF, no. 328826.

-
- [1] I. Allekotte *et al.* (Pierre Auger Collaboration), Nucl. Instrum. Meth. A **586**, 409 (2008).
 - [2] J. Abraham *et al.* (Pierre Auger Collaboration), Nucl. Instrum. Meth. A **620**, 227 (2010).
 - [3] H. Kawai *et al.*, Nucl. Phys. B (Proc. Suppl.) **175-176**, 221 (2008).
 - [4] J. Matthews, Astropart. Phys. **22**, 387 (2005).
 - [5] I.C. Mariş, PhD thesis, Karlsruhe University (2008).
 - [6] J. Abraham *et al.* (Pierre Auger Collaboration), Phys. Lett. B **685**, 239 (2010).
 - [7] T. Abu-Zayyad *et al.* (Telescope Array Collaboration), Astrophys. J. **768**, L1 (2013).
 - [8] A. Aab *et al.* (Pierre Auger Collaboration), JCAP **08**, 019 (2014).
 - [9] P.M. Hansen, J. Alvarez-Muniz, and R.A. Vazquez, Astropart. Phys. **34**, 503–512 (2011).
 - [10] H.P. Dembinski, PhD thesis, RWTH Aachen (2009).
 - [11] R. Ulrich *et al.*, Phys. Rev. D **83**, 054026 (2011).
 - [12] J. Hersil *et al.*, Phys. Rev. Lett. **6**, 22 (1961).
 - [13] F. James, *Statistical Methods in Experimental Physics*, World Scientific Publishing, Singapore (2006).
 - [14] G. Cowan, *Statistical Data Analysis*, Clarendon Press, Oxford (1998).
 - [15] H.P. Dembinski and M. Roth, Nucl. Instrum. Meth. A **729**, 410 (2013).
 - [16] M.J. Tueros *et al.* (Pierre Auger Collaboration), Proc. 33rd Int. Cosmic Ray Conf., Rio de Janeiro, Brazil (2013), <http://arxiv.org/abs/1307.5059>.
 - [17] A. Aab *et al.* (Pierre Auger Collaboration), Phys. Rev. D **91**, 032003 (2015).
 - [18] H.P. Dembinski *et al.*, Astropart. Phys. **34**, 128 (2010).
 - [19] R. Pesce, Proc. 32nd Int. Cosmic Ray Conf., Beijing, China (2011), <http://arxiv.org/abs/1107.4809>.
 - [20] H.P. Dembinski, Proc. 32nd Int. Cosmic Ray Conf., Beijing, China (2011), <http://arxiv.org/abs/1107.4809>.
 - [21] B. Efron and R. Tibshirani, *An Introduction to the Bootstrap*, Chapman and Hall, New York (1993).

Appendix A: Expectation of $g_S^N(\hat{S}; \bar{S})$ and $g_S(\hat{S}; \bar{S})$

We compute the expectation value of Eq. (13) and Eq. (14). The experimental conditions that we consider are $\hat{S}/\sigma[\hat{S}] \gg 0$ and $\bar{S}/\sigma[\bar{S}] \gg 0$. This allows us to compute the expectation value over the whole domain of real numbers in good approximation. The expectation

value for Eq. (14) immediately follows

$$E[\hat{S}] = \int_{-\infty}^{\infty} d\hat{S} \hat{S} g_s^N(\hat{S}; \bar{S}) = \bar{S}, \quad (\text{A1})$$

since $g_s^N(\hat{S}; \bar{S})$ is a normal distribution around \bar{S} .

For the computation of the expectation value of Eq. (13), we use that by definition the expectation values of $g_s(\hat{S}; S)$ and $s(S; \bar{S})$ are S and \bar{S} , respectively. By changing the order of integration, we obtain

$$E[\hat{S}] = \int_{-\infty}^{\infty} d\hat{S} \hat{S} \int_{-\infty}^{\infty} dS g_s(\hat{S}; S) s(S; \bar{S}) \quad (\text{A2})$$

$$= \int_{-\infty}^{\infty} dS s(S; \bar{S}) \int_{-\infty}^{\infty} d\hat{S} \hat{S} g_s(\hat{S}; S) \quad (\text{A3})$$

$$= \int_{-\infty}^{\infty} dS s(S; \bar{S}) S = \bar{S}. \quad (\text{A4})$$

Appendix B: Toy simulation of calibration data

We make a Monte-Carlo simulation of Eq. (6) to obtain artificial calibration data. We start by simulating the arrival distribution $h(E, \theta) = h_E(E) h_\theta(\theta)$ of air showers at the detector aperture. The events generated here simulate highly-inclined events with $60^\circ < \theta < 80^\circ$, as they are seen by the Pierre Auger Observatory. In the numerical formulas that follow, the energy E is in units of eV, the zenith angle θ in units of radian.

The energy spectrum h_E is modeled by a broken power law with a low-energy suppression that takes the form of the cumulative normal distribution. The zenith-angle spectrum h_θ is modeled as modified exponential decay,

$$h_E(E) \propto \text{erfc} \left(-\frac{\lg E - p_0}{\sqrt{2}p_1} \right) \times \\ \times \begin{cases} E^{p_2-0.3} & ; \text{if } 17.0 < \lg E \leq 18.3, \\ E^{p_2} & ; \text{if } 18.3 < \lg E \leq 19.6, \\ E^{p_2-1.2} & ; \text{if } 19.6 < \lg E, \end{cases} \\ h_\theta(\theta) \propto \exp(p_3 z + p_4 z^2), \quad z = \theta - 1.047, \\ \mathbf{p} = (18.3, 0.3, -2.3, -6.4, -45.0).$$

The shower-to-shower fluctuations are taken to be normal-distributed and with a constant relative resolution $\sigma_S/\bar{S} = 0.15$.

The detector-generated fluctuations for the energy estimate \hat{E} and the size estimate \hat{S} are drawn from normal distributions with relative resolutions,

$$\sigma_{\hat{E}}/E = \begin{cases} p_0 + p_1(\lg E - 18.4)^2 & ; \text{if } \lg E \leq 18.4, \\ p_0 & ; \text{otherwise,} \end{cases} \\ \sigma_{\hat{S}}/S = p_2 + p_3/\sqrt{S}, \\ \mathbf{p} = (0.10, 0.03, 0.04, 0.10).$$

The reconstruction codes in the real experiment provide event-wise estimates of these resolutions, which are used by fits. The estimates randomly vary around the true resolutions. To simulate this, we multiply the true resolutions that are used internally with a factor $(1 + 0.1z)$ before they are passed on to the fits, where z is standard normal-distributed.

The reduced trigger efficiency for small air-shower sizes is included in the toy simulation. The trigger probability has the form of a cumulative normal distribution,

$$P(\hat{S}, \theta) = \frac{1}{2} \text{erfc} \left(\frac{\lg \hat{S} - \mu(\theta)}{\sqrt{2}\sigma(\theta)} \right), \\ \mu(\theta) = (1 - z)p_0 + zp_1, \quad z = \theta/0.35, \\ \sigma(\theta) = (1 - z)p_2 + zp_3, \quad z = \theta/0.35, \\ \mathbf{p} = (-0.95, -1.3, 0.2, 0.6).$$

The probability is taken to be a function of the size estimate \hat{S} , not S , since the trigger decision is highly correlated with the sampling fluctuations of \hat{S} around the true size S . The reduced trigger efficiency of the energy measurement is effectively included in the energy distribution $h_E(E)$ and not simulated separately.